Response of a Li-glass/multi-anode photomultiplier detector to α-particles from ^{241}Am

E. Rofors [a,b], H. Perrey [a,b], R. Al Jebali [b,c], J.R.M. Annand [c], L. Boyd [c], U. Clemens [g], S. Desert [e], R. Engels [f], K.G. Fissum [a,b,*], H. Frielinghaus [f], C. Gheorghe [h], R. Hall-Wilton [b,d], S. Jaksch [f], A. Jalgén [a], K. Kanaki [b], G. Kemmerling [f], V. Maulerova [a], N. Mauritzson [a], R. Montgomery [c], J. Scherzinger [a,b,1], B. Seitz [c]

[a] *Division of Nuclear Physics, Lund University, SE-221 00 Lund, Sweden*
[b] *Detector Group, European Spallation Source ERIC, SE-221 00 Lund, Sweden*
[c] *SUPA School of Physics and Astronomy, University of Glasgow, Glasgow G12 8QQ, Scotland, UK*
[d] *Mid-Sweden University, SE-851 70 Sundsvall, Sweden*
[e] *LLB, CEA, CNRS, Université Paris-Saclay, 91191 Gif-sur-Yvette, France*
[f] *Jülich Centre for Neutron Science JCNS, Forschungszentrum Jülich, D-52425 Jülich, Germany*
[g] *Zentrum für Anwendungsentwicklung und Elektronik ZEA-2, Forschungszentrum Jülich, D-52425 Jülich, Germany*
[h] *Integrated Detector Electronics AS, Gjerdrums vei 19, NO-0484 Oslo, Norway*

ARTICLE INFO

ABSTRACT

The response of a position-sensitive Li-glass scintillator detector to α-particles from a collimated ^{241}Am source scanned across the face of the detector has been measured. Scintillation light was read out by an 8×8 pixel multi-anode photomultiplier and the signal amplitude for each pixel has been recorded for every position on a scan. The pixel signal is strongly dependent on position and in general several pixels will register a signal (a hit) above a given threshold. The effect of this threshold on hit multiplicity is studied, with a view to optimize the single-hit efficiency of the detector.

1. Introduction

The European Spallation Source (ESS) [1] will soon commence operations as the most powerful neutron source in the world. Highly efficient, position-sensing neutron detectors are crucial to the scientific mission of ESS. The worldwide shortage of ^{3}He [2–4] has resulted in considerable effort being undertaken to develop new neutron-detector technologies. One such effort is the development of Solid-state Neutron Detectors SoNDe [5–7] for high-flux applications, motivated by the desire for two-dimensional position-sensitive systems for small-angle neutron-scattering experiments [8–17]. The SoNDe concept features individual neutron-detector modules which may be easily configured to instrument essentially any experimental phase space. The specification for the neutron interaction position reconstruction accuracy for the SoNDe technology is 6 mm.

The core components of a SoNDe module are the neutron-sensitive Li-glass scintillator and the pixelated multi-anode photomultiplier tube (MAPMT) used to collect the scintillation light. The response of MAPMTs to scintillation-emulating laser light has been extensively studied [18–26]. Similar Li-glass/MAPMT detectors have been tested

with thermal neutrons [27] and a SoNDe detector prototype has been evaluated in a reactor-based thermal-neutron beam [6]. In this paper, we present results obtained for the response of a SoNDe detector prototype to α-particles from a collimated ^{241}Am source scanned across the face of the scintillator. Our goal was to examine methods to optimize the localization of the scintillation signal with a view to optimizing the position resolution of the detector, under constraints imposed by envisioned readout schemes for the detector. We were particularly interested in the behavior of the SoNDe detector prototype at the vertical and horizontal boundaries between the pixels and the corners where four pixels meet.

2. Apparatus

2.1. Collimated α-particle source

Fig. 1 shows a sketch of the assembly used to produce a beam of α-particles. It consisted of a ^{241}Am α-particle source mounted in a 3D-printed holder/collimator assembly.

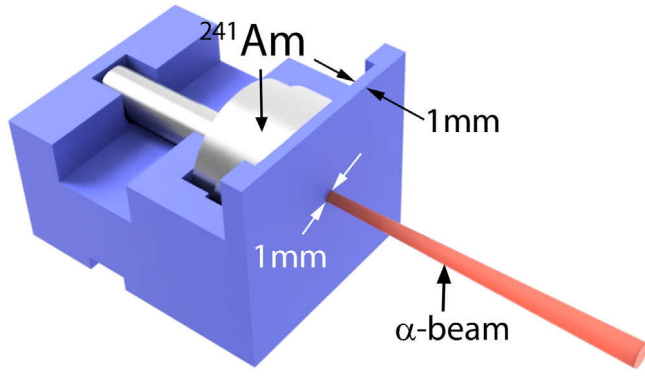**Fig. 1.** [241]Am α-particle source mounted in the holder/collimator assembly used to define a beam of α-particles. The radioactive source fit sungly in the blue holder/collimator. The assembly shown has a 1 mm thick face plate and a 1 mm diameter hole, resulting in the diverging red beam of α-particles. (For interpretation of the references to color in this figure legend, the reader is referred to the web version of this article.)
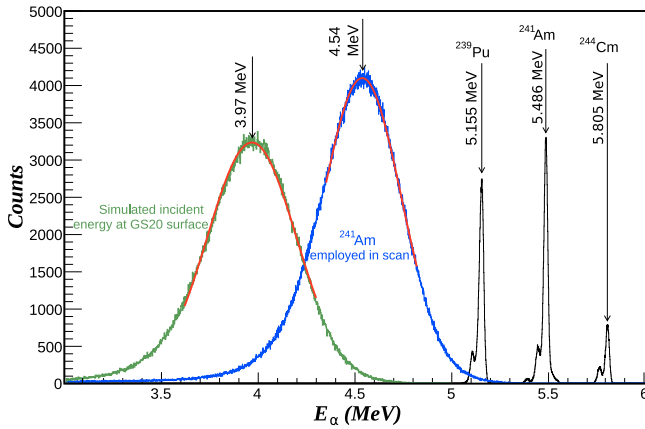
Fig. 2. Uncollimated α-particle spectrum (in vacuum) emitted by the [241]Am source employed in the suite of measurements reported on here (broad blue distribution) together with a red fitted Gaussian function (indicating peaking at 4.54 MeV) and a triple α-particle spectrum emitted by a very thin-windowed three-actinide calibration source (sharp black primary peaks at 5.155 MeV, 5.486 MeV, and 5.805 MeV). The spectrum depicted in green is a GEANT4 simulation of the α-particle spectrum incident on the GS20 wafer, peaking at 3.97 MeV. (For interpretation of the references to color in this figure legend, the reader is referred to the web version of this article.)

The α-particle emission energies of [241]Am are 5.5 MeV (∼85%) and 5.4 MeV (∼15%). The gamma-ray background from the subsequent decay of excited states of [237]Np has an energy of ∼60 keV and has a negligible effect on the α-particle response of the SoNDe detector prototype. The α-particle spectrum from the present source was measured (Fig. 2) using a high-resolution passive-implanted planar silicon (PIPS) detector system in vacuum, where the PIPS detector was calibrated using a three-actinide calibration source. The average energy of the α-particles emitted by the presently employed source was ∼4.5 MeV, corresponding to an energy loss of ∼1 MeV in the source window.

Holder/collimator assemblies for the [241]Am source were 3D-printed from polyactic acid using the fused deposition modeling technique. For our measurements, we used 1 mm thick collimators with either 3 mm (for gain mapping) or 1 mm (for border scanning) diameter apertures, resulting in uniform 3 mm or 1 mm irradiation spots at the upstream face of the scintillator. The distance from the [241]Am source to this upstream face was 6 mm of air. GEANT4 simulation showed that the mean α-particle energy at the surface of the GS20 wafer was ∼4.0 MeV, in excellent agreement with the results of Ref. [28].

2.2. SoNDe detector prototype

The SoNDe detector prototype investigated in this paper is being developed for large-area arrays to detect thermal to cold neutrons with energies of ≤25 meV. It consists of a 1 mm thick lithium-silicate scintillating glass wafer coupled to a H12700A MAPMT.

2.2.1. Li-glass scintillator

Cerium-activated lithium-silicate glass scintillator GS20 [29–32] purchased from Scintacor [33] was chosen for this application. GS20 has been demonstrated to be an excellent scintillator for the detection of thermal and cold neutrons and arrays of scintillator tiles can be arranged into large area detector systems [8–11,13]. The lithium content is 6.6% by weight, with a 95% [6]Li isotopic enhancement, giving a [6]Li concentration of 1.58×10^{22} atoms/cm^3. [6]Li has a thermal-neutron capture cross section of ∼940 b at 25 meV, so that a 1 mm thick wafer of GS20 detects ∼75% of incident thermal neutrons. The process produces a 2.05 MeV α-particle and a 2.73 MeV triton which have mean ranges of 5.3 μm and 34.7 μm respectively [34] in GS20. Using the present α-particle source, scintillation light was generated overwhelmingly within ∼15 μm of the upstream face of the scintillating wafer. The large stopping power of 4.0 MeV α-particles prohibited the use of a reflector on the upstream side of the scintillating wafer. We note that the scintillation light-yield outputs for 1 MeV protons is ∼5 times higher than that of 1 MeV α-particles [35]. Thus, after thermal-neutron capture, the triton will produce a factor of ∼5 more scintillation light than the α-particle. Tests by van Eijk [36] indicate ∼6600 scintillation photons per neutron event with a peak at a wavelength of 390 nm, which corresponds to ∼25% of the anthracene benchmark. The sensitivity of GS20 to gamma-rays is energy dependent. A threshold cut will eliminate the low-energy gamma-rays, but higher-energy gamma-rays can produce large pulses if the subsequent electrons (from Compton scattering or pair production) traverse sufficient thickness of GS20.

Our glass wafer was 1 mm thick and 50 mm × 50 mm in area. The glass faces, apart from the edges, were polished and the wafer was fitted to the MAPMT window without any optical coupling medium and held in place with tape along the thin wafer edges. The index of refraction of GS20 is 1.55 at 395 nm. We have assumed that the [6]Li distribution in our scintillating wafer was uniform.

2.2.2. Multi-anode photomultiplier tube

The Hamamatsu type H12700A borosilicate glass MAPMT employed in the SoNDe detector prototype is an 8 × 8 pixel device with outer dimensions 52 mm × 52 mm and an active cathode area of 48.5 mm × 48.5 mm, resulting in a packing density of 87%. The bialkali photocathode produces a peak quantum efficiency of ∼33% at ∼380 nm wavelength, which is well matched to the GS20 scintillation. Compared to its predecessor type H8500 MAPMT, the H12700A MAPMT achieves similar overall gain, but with 10 as opposed to 12 dynode stages. The H12700A MAPMT employed for the present tests had a gain of 2.09×10^6 and a dark current of 2.67 nA at an anode–cathode potential of −1000 V. Each of the 64 ∼6 × 6 mm^2 pixels in the Hamamatsu H12700A MAPMT has a slightly different gain, which is measured and documented by the supplier. A typical H12700A MAPMT has a factor 2 variation in pixel gain (factor 3 worst case) [37]. The datasheet provided by Hamamatsu for the H12700A MAPMT used in this study had a worst case anode-to-anode gain difference of a factor 1.7. Fig. 3 shows a photograph of the device together with a pixel map.

3. Measurement

The SoNDe detector prototype was irradiated using the collimated beams of α-particles (Section 2.1) where the center of the beam was directed perpendicular to the face of the GS20 wafer. The total flight distance of α-particles through air to the surface of the GS20 wafer was 6 mm (Fig. 1). The downstream face of the source holder/collimator assembly was translated parallel to the surface of the scintillator wafer on
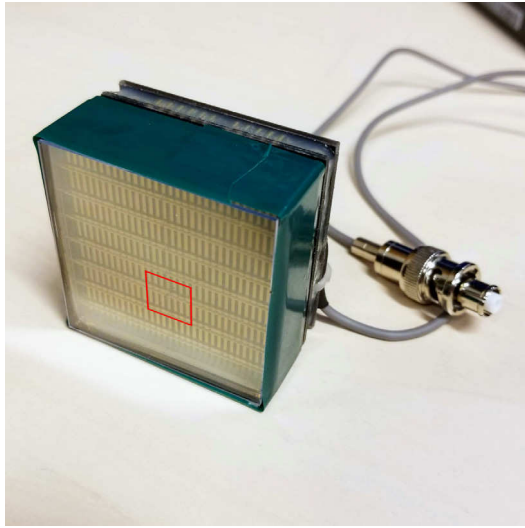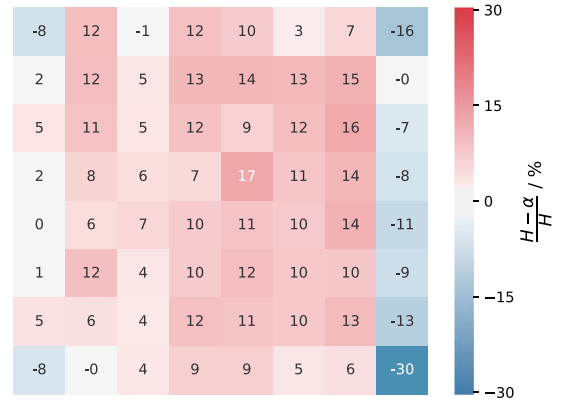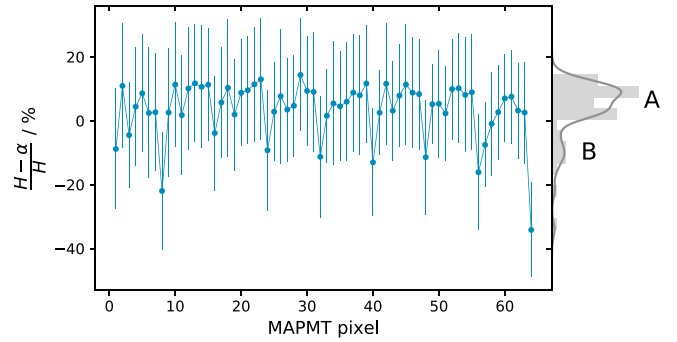
(a) MAPMT with scintillator
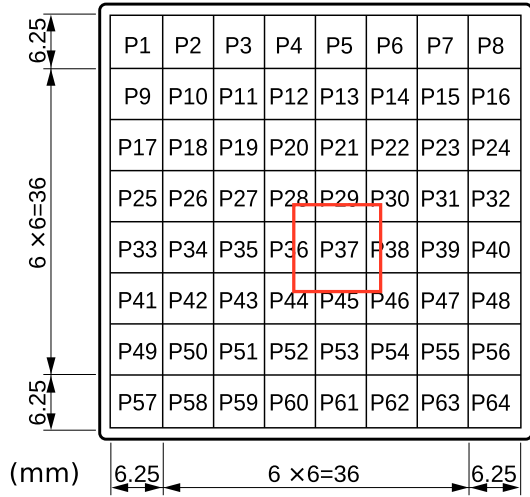
(b) MAPMT pixel map

Fig. 3. The Hamamatsu H12700A MAPMT. 3(a): Photograph of the MAPMT together with the GS20 scintillator wafer. 3(b): Numbering of the 64 MAPMT pixels (front view). Pixel 1 (P1) is located in the top left-hand corner of the MAPMT looking into it from the front. Sketch from Ref. [37]. The red boxes indicate the region of irradiation reported on in detail in this paper. (For interpretation of the references to color in this figure legend, the reader is referred to the web version of this article.)
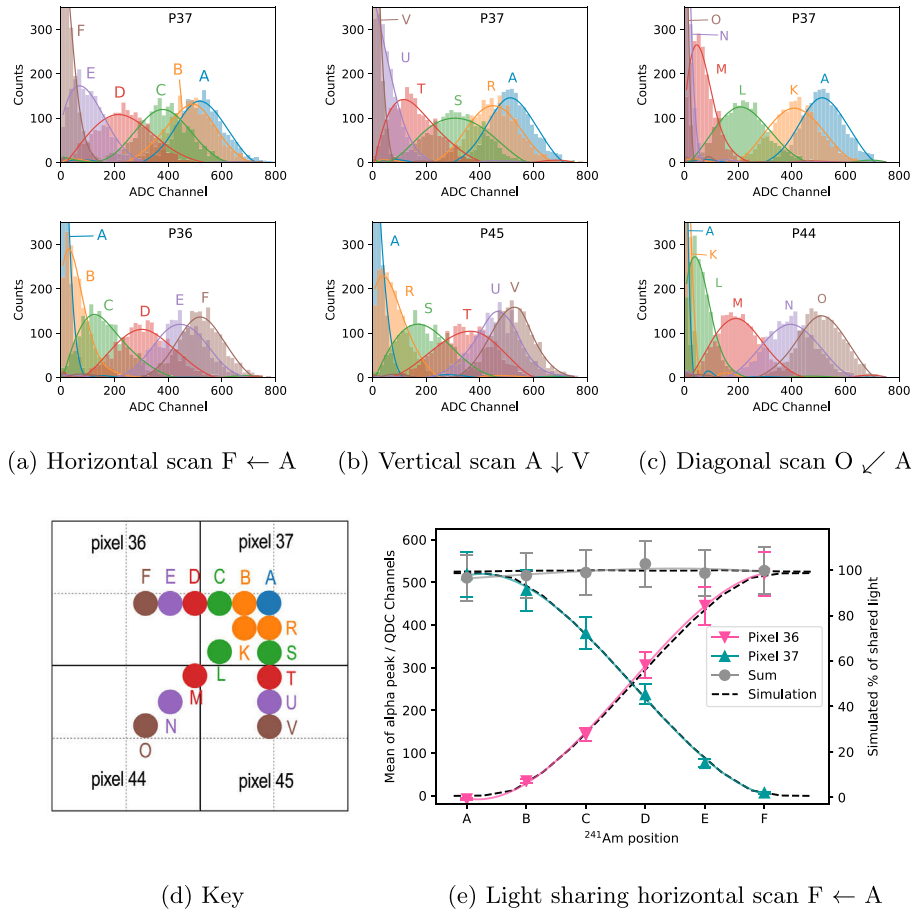

(a) Gain differences, areal

(b) Gain differences, projected

Fig. 4. Differences between the α-scan gain-map and the Hamamatsu gain-map normalized to the Hamamatsu gain-map in percent. 4(a): 2D representation in which the top-left corner corresponds to P1. 4(b): 1D representation of the same as a function of pixel. Error bars are derived from fit widths. The values have been joined with a line to guide the eye. A histogram of the gain differences is projected in gray on the right vertical axis. Cluster A of that histogram corresponds to red pixels in 4(a) while cluster B corresponds to blue pixels. (For interpretation of the references to color in this figure legend, the reader is referred to the web version of this article.)

an XY-coordinate scanner powered by a pair of Thorlabs NRT150 stepping motors [38]. This was programmed to scan a lattice of irradiation points uniformly distributed across the face of the device. The entire assembly was located within a light-tight box and the temperature (~25°), pressure (~101.3 kPa), and humidity (~30%) within the box were logged at the beginning and end of each measurement position. The anode signals from each of the pixels in the MAPMT were recorded using standard NIM and VME electronics. The positive polarity dynode-10 signal was shaped and inverted using an ORTEC 454 NIM timing filter amplifier producing a negative polarity signal with risetime ~5 ns, falltime ~20 ns, and amplitude some tens of mV, which was fed to an ORTEC CF8000 constant-fraction discriminator set to a threshold of −8 mV. The resulting NIM logic pulses with a duration of 150 ns provided a trigger for the data-acquisition system and a gate for the CAEN V792 VME charge-to-digital converters (QDCs) used to record the 64 anode pixel charges. A CAEN V2718 VME-to-PCI optical link bridge was used to sense the presence of a trigger signal and to connect

the VMEbus to a Linux PC-based data-acquisition system. The digitized signals were recorded on disk and subsequently processed using ROOT-based software [39]. Data were recorded for ~120 s at each point on a scan, so that in total a scan could take several hours.

4. Results

The gain-calibration datasheet provided by Hamamatsu may be used to correct for non-uniform response. However, previous work [18–23,25] has clearly suggested that mapping of pixel gains is highly dependent upon the irradiation conditions. Since our α-particle beam results in very short (~10 s of ns) pulses of highly localized scintillation light which are in sharp contrast to the steady-state irradiation measurement employed by Hamamatsu, we re-measured the gain-map of our MAPMT *in situ* using the equipment described previously. For each pixel, the 3 mm diameter α-particle collimator was centered on the XY position of the pixel center of the MAPMT photocathode and 2200 α-particle events were recorded. The resulting anode-charge distributions were well fitted with Gaussian functions (average χ^2 per degree of freedom 1.50 with a variance of 0.14) and the means, μ, and standard deviations, σ, were recorded. The largest measured μ-value

(a) Horizontal scan F ← A   (b) Vertical scan A ↓ V   (c) Diagonal scan O ↙ A

(d) Key   (e) Light sharing horizontal scan F ← A

Fig. 5. 5(a)–5(c) Measured charge distributions for four adjacent pixels as the α-particle beam was translated in 1 mm horizontal and vertical steps across the pixel boundaries. (a): horizontal scan from P37 to P36. (b): vertical scan from P37 to P45. (c): diagonal scan from P37 to P44. 5(d): Key. The solid (dashed) black lines indicate the pixel boundaries (centers). 5(e): Gain-corrected means of the collected charge distributions corresponding to 5(a). The curves are splines drawn to guide the eye. Error bars correspond to $\sigma/10$. (For interpretation of the references to color in this figure legend, the reader is referred to the web version of this article.)

(corresponding to the pixel with the highest gain) was normalized to 100. The relative difference between the Hamamatsu gain-map values, H, and the α-scanned gain-map values, α, was calculated as $\frac{H-\alpha}{H}$ on a pixel-by-pixel basis. Fig. 4 shows the results of our gain-map measurement, where the present results show significant differences to the Hamamatsu measurement. General trends in regions of high and low gain agree. Measurements of a sample of 30 H12700A MAPMTs revealed that the window face is not flat and was systematically ∼80 μm lower at the center compared to the edges. The non-uniformity of the air gap between the GS20 and MAPMT window may be a partial cause of the gain discrepancy displayed in Fig. 4, as may reflections at the edges of the GS20 wafer. In the following, we use the present α-scintillation generated gain-map, which in principle will embody non-uniform light-collection effects. Nonetheless, scintillation-light propagation through the SoNDe detector prototype is being studied in a GEANT4-based simulation [40,41] in order to better understand these effects.

Fig. 5 shows the positions of the 1 mm collimated α-particle source employed for the horizontal, vertical, and diagonal XY scans. The positions are labeled A–V and color coded (5(d)). The α-particle pulse-height spectra recorded at each of the scan positions are displayed in 5(a)–5(c) for pixels P36, P37, P44, and P45 which encompass the scan coordinates. The QDC pulse-height distributions have been pedestal subtracted and corrected for non-uniform pixel gain (Fig. 4). It is obvious that the efficiency of scintillation light collection in a single pixel is strongly dependent on the position of the α-particle interaction. The signal amplitude is maximized when light is produced at the center of the pixel. This variation in amplitude with position may be seen more

clearly in 5(e), which shows the mean of the pulse-height distributions as a function of interaction position for the horizontal scan (5(a)). The full curves are splines to guide the eye, while the dashed curves display the predictions of a ray-tracing simulation of light propagation [42]. The simulation is in good agreement with the measured data. After gain correction, these distributions should be symmetric about the pixel boundary locations. The system was aligned such that position D should have corresponded to the boundary between P36 and P37. However, the fits to the data suggest that the scan positions were offset by 0.2 mm to the left (Fig. 5(e)). Corresponding fits to the vertical-scan data show a 0.4 mm vertical offset. The sum of the means of the two adjacent pixels scanned is also displayed. This shows that the amount of light collected by the two pixels over which the scan is performed is independent of position.

In general, several pixels adjacent to the target pixel will collect some scintillation light and in principle, this could be used to better localize the position of the scintillation as in an Anger camera [43,44]. While possible, this will not be the standard mode of operation for SoNDe modules running at ESS due to data-volume limitations. For production running at ESS, MAPMT pixels will be read and time-stamped on an event-by-event basis as lying either above or below per-pixel discriminator thresholds.

The multiplicity of pixels with a signal above discriminator threshold (the hit multiplicity denoted $M = 1$, $M = 2$, etc.) has been investigated as a function of the scintillation position and also the discrimination level. The investigation involved a 10×10 measurement matrix (100 runs total) of collimated α-particle irradiations, with 2000 events in each run. Fig. 6 displays regions in the vicinity of P37 where

(a) Key

(b) Threshold 100 QDC channels

(c) Threshold 235 QDC channels

(d) Threshold 500 QDC channels
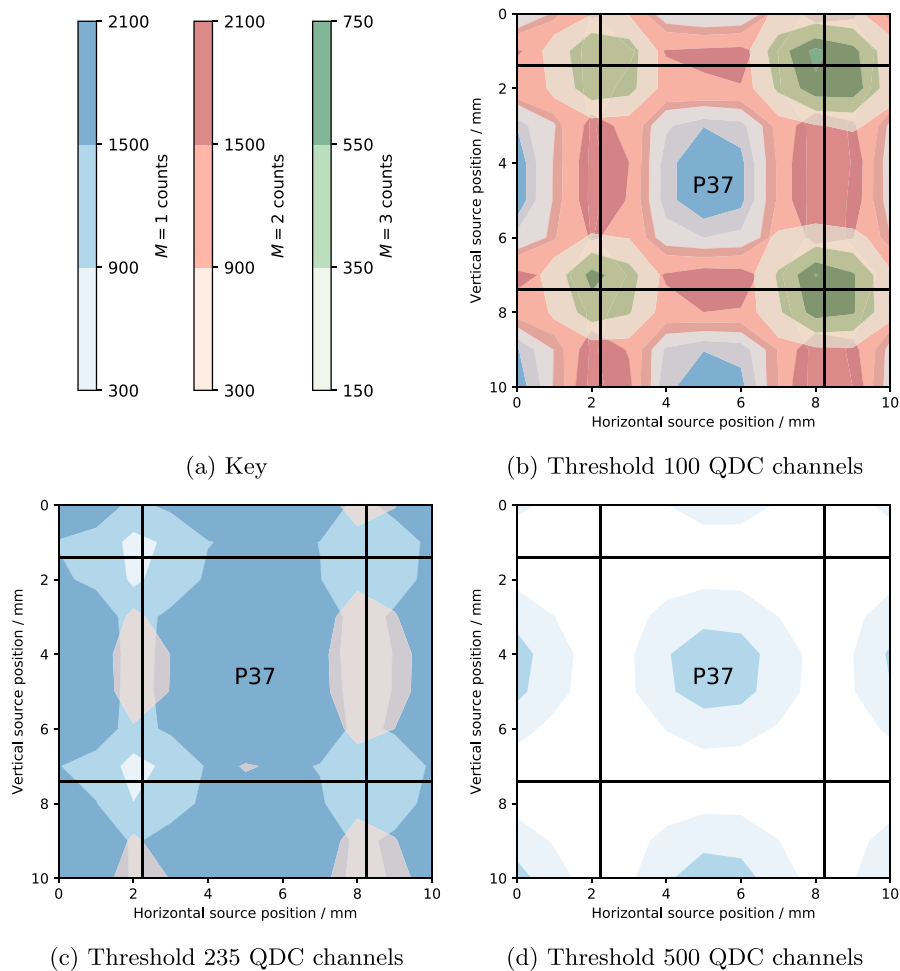
Fig. 6. Contour plots of the multiplicity distributions for pixels lying near P37 for different thresholds as a function of α-particle beam irradiation location. The black lines denote the pixel boundaries. In all three contour plots, blues indicate $M = 1$ events, reds indicate $M = 2$ events, and greens indicate $M = 3$ events. The lighter the shade of the color, the fewer the counts. (For interpretation of the references to color in this figure legend, the reader is referred to the web version of this article.)

$M = 1$, 2, and 3 predominate. Hits have been determined according to the pulse heights (Fig. 5) exceeding discrimination levels of 100 (6(b)), 235 (6(c)), and 500 (6(d)) QDC channels. At the 100-channel threshold, $M = 1$ events are confined to the center of a pixel. At the edges, events are predominantly $M = 2$, while in the corners, $M = 3$. To see any considerable $M = 4$ contributions around the pixel corners, lower thresholds are required as seen in Fig. 7. Raising the threshold to 235 channels extinguishes $M = 2$ and $M = 3$ almost completely. Raising even further to 500 channels serves merely to reduce the number of $M = 1$ events. The threshold level obviously affects the relative efficiency with which the SoNDe detector prototype registers $M = 1$, $M = 2$, etc. events, and Fig. 6 clearly shows that there is an optimum threshold value to maximize the number of $M = 1$ events detected and also to maximize the area of the detector where the $M = 1$ efficiency is high.

Fig. 7 illustrates the trend in M as a function of QDC threshold cut when a series of 36 α-particle beam measurements were performed in a 6×6 grid covering the face of P37. Variable thresholds have been applied to the data, but in each case, the same cut has been applied to all pixels. Two "extreme" curves are shown in 7(a): the $M = 0$ curve and the $M > 4$ curve. The $M = 0$ curve corresponds to events which do not exceed the applied threshold in any pixel. $M = 0$ events start to register at a threshold of ∼30 channels and rise steeply after channel ∼200 to ∼95% at channel 600. The $M > 4$ curve corresponds to events which exceed the applied threshold in four or more pixels. At a threshold of ∼4 channels, ∼90% of events are $M > 4$, falling essentially to zero at channel ∼50. Four other curves are shown in 7(b): $M = 1$,

$M = 2$, $M = 3$, and $M = 4$, corresponding to events which exceed the applied threshold in one, two, three, and four pixels, respectively. Each of these curves demonstrate clear maxima so that the analysis procedure may be "tuned" to select an event multiplicity by applying the appropriate threshold. The detection efficiency for $M = 1$ events peaks at ∼75% at a threshold of 235 channels, where $M = 2$, 3, and 4 have negligible efficiency as they peak at channels 65, 25, and 18, respectively.

5. Summary and discussion

The position-dependent response of a SoNDe detector prototype, which consists of a 1 mm thick wafer of GS20 scintillating glass read out by an 8×8 pixel type H12700A MAPMT has been measured using a collimated ^{241}Am source. The spreading of the scintillation light and the resulting distributions of charge on the MAPMT anodes were studied as a function of α-particle interaction position by scanning the collimated α-particle beam across the face of the MAPMT using a high precision XY coordinate translator.

Initially, pixel gain non-uniformity across the 64 MAPMT anodes was measured using a 3 mm collimated source positioned at each pixel center, which produced uniform illumination of the pixel centers. The results, which differ from relative gain data provided by the MAPMT manufacturer on the 10% level (Fig. 4), were used to correct all subsequent 1 mm scan data.

Anode charge distributions collected from each MAPMT pixel at each scanned coordinate show a strong position dependence of the
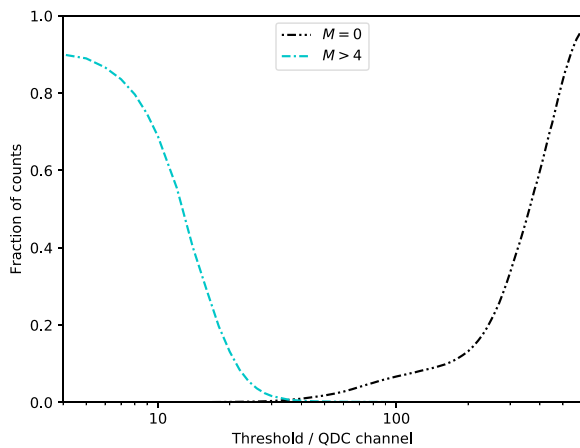
(a) Extreme multiplicities
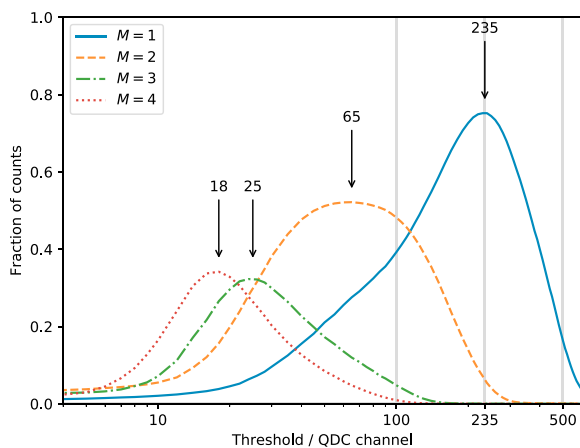
(b) Practical multiplicities

Fig. 7. Tuning the analysis using a single QDC threshold. Relationships between the relative number of events and threshold. Top Panel: $M = 0$ (black dot–dot-dashed line) and $M > 4$ (light blue dot-dashed line). Bottom Panel: $M = 1$ (dark blue solid line), $M = 2$ (orange dashed line), $M = 3$ (green dot-dashed line), and $M = 4$ (red dotted line). The gray vertical lines at QDC channel 100, 235, and 500 represent three of the QDC threshold cuts employed in Fig. 6. Arrows indicate the optimal values for QDC threshold cuts for tuning the resulting data set for a specific value of M. (For interpretation of the references to color in this figure legend, the reader is referred to the web version of this article.)

signal amplitude. The single-pixel signal is strongest when the source is located at the pixel center, and falls away as the pixel boundaries are approached (Fig. 5). At the pixel center, the signal tends to be concentrated in that pixel, while at pixel boundaries, the signal is shared between the adjacent pixels.

Rate and data-volume considerations for operation of SoNDe modules at ESS will require a relatively simple mode of operation for the SoNDe data-acquisition system. It will not be possible to read out multiple pixels to construct a weighted-mean interaction position as in an Anger Camera. Instead, it will be necessary to identify the pixel where the maximum charge occurs and record only the identity (P1–P64) of that pixel. To this end, we studied the effect of signal amplitude thresholds on the multiplicity of pixel hits (that is, the number of signals above threshold) as a function of the α-particle interaction position (Fig. 6). This study showed that there is an optimum discrimination level which maximizes the number of single-pixel or $M = 1$ hits. Below this level, multi-pixel hits start to dominate, while above this level, the

single-pixel efficiency drops (Fig. 7). At the optimum discrimination level, which under the present operating conditions was channel 235, ∼75% of the α-particle interactions were registered as single pixel.

Further work pertaining to the characterization of the SoNDe detector prototype is progressing in parallel to the project reported here. This includes the development of a simulation within the GEANT4 framework to complement and extend the ray-tracing simulation mentioned in this work. This GEANT4 model fully simulates the interactions of ionizing radiation in the GS20 and tracks the produced scintillation photons to the MAPMT cathode. It is being used to study the effects of optical coupling, surface finish, and partial pixelation (by machining grooves) of the GS20 wafer on the response of the detector. The present results, along with other measurements of the scintillator response will be used to test the predictions of the GEANT4-based model of the SoNDe detector prototype. The relative response of a SoNDe detector prototype to different incident particle species is also being studied. Irradiation of a SoNDe detector prototype with a collimated beam of thermal neutrons has been performed and data analysis is nearing completion. An extension of these studies for possible non-ESS applications of the SoNDe detector prototype, where an optical diffuser is inserted between the GS20 and the MAPMT, is planned to examine a possible Anger camera mode of operation. And further position-dependence studies will be made using fine needle-like beams of a few MeV protons and deuterons produced by an accelerator. This will allow determination of the scintillation signal as a function of interacting particle species and will be complemented by work with fast-neutron and gamma-ray sources.

References

[1] The European Spallation Source, https://europeanspallationsource.se/.
[2] R.T. Kouzes, PNNL-18388 Pacific Northwest National Laboratory, Richland, WA, 2009.
[3] D.A. Shea, D. Morgan, Congressional Research Service, Technical Report R41419, 2010.
[4] K. Zeitelhack, Neutron News 23 (4) (2012) 1013.
[5] Solid-State Neutron Detector, https://cordis.europa.eu/project/rcn/194934_en.html.
[6] S. Jaksch, et al., Proc int. conf. neutron optics (NOP2017), JPS Conf. Proc. 22 (2018) 011019, http://dx.doi.org/10.7566/JPSCP.22.011019.
[7] G. Kemmerling, S. Jaksch, Forschungszentrum Jülich, Solid-State Neutron Detector INFRADEV-1-2014/H2020, Grant Agreement Number: 654124.
[8] M. Heiderich, et al., Nucl. Instrum. Methods Phys. Res. A 305 (1991) 423, http://dx.doi.org/10.1016/0168-9002(91)90562-5.
[9] G. Kemmerling, et al., IEEE Trans. Nucl. Sci. 48 (2001) 1114, http://dx.doi.org/10.1109/23.958733.
[10] G. Kemmerling, et al., IEEE Trans. Nucl. Sci. 51 (2004) 1098, http://dx.doi.org/10.1109/TNS.2004.829576.
[11] G. Kemmerling, et al., IEEE Nucl. Sci. Symp. Conf. (2003) 722, Rec 03CH37515, http://dx.doi.org/10.1109/NSSMIC.2003.1351801.
[12] S. Jaksch, et al., Nucl. Instrum. Methods Phys. Res. A 762 (2014) 22, http://dx.doi.org/10.1016/j.nima.2014.04.024.
[13] A.V. Feoktystov, et al., J. Appl. Crystallogr. 48 (2015) 61, http://dx.doi.org/10.1107/S1600576714025977.
[14] R. Engels, et al., IEEE Trans. Nucl. Sci. 44 (3) (1997) http://dx.doi.org/10.1109/23.603701.
[15] R. Engels, et al., IEEE Trans. Nucl. Sci. 45 (3) (1998) http://dx.doi.org/10.1109/NSSMIC.1997.672706.

[16] R. Engels, et al., IEEE Trans. Nucl. Sci. 46 (4) (1999) http://dx.doi.org/10.1109/23.790694.

[17] R. Engels, et al., IEEE Trans. Nucl. Sci. 49 (3) (2002) http://dx.doi.org/10.1109/23.790694.

[18] S. Korpar, et al., Nucl. Instrum. Methods Phys. Res. A 442 (2000) 316, http://dx.doi.org/10.1016/S0168-9002(99)01242-5.

[19] K. Rielage, et al., Nucl. Instrum. Methods Phys. Res. A 463 (2001) 149, http://dx.doi.org/10.1016/S0168-9002(01)00448-X.

[20] T. Matsumoto, et al., Nucl. Instrum. Methods Phys. Res. A 521 (2004) 367, http://dx.doi.org/10.1016/j.nima.2003.11.384.

[21] K. Lang, et al., Nucl. Instrum. Methods Phys. Res. A 545 (2005) 852, http://dx.doi.org/10.1016/j.nima.2005.02.041.

[22] P. Abbon, et al., Nucl. Instrum. Methods Phys. Res. A 595 (2008) 177, http://dx.doi.org/10.1016/j.nima.2008.07.074.

[23] R.A. Montgomery, et al., Nucl. Instrum. Methods Phys. Res. A 695 (2012) 326, http://dx.doi.org/10.1016/j.nima.2011.11.026.

[24] Rachel Ann Montgomery, Nucl. Instrum. Methods Phys. Res. A 732 (2013) 732, http://dx.doi.org/10.1016/j.nima.2013.08.012.

[25] R.A. Montgomery, et al., Nucl. Instrum. Methods Phys. Res. A 790 (2015) 28, http://dx.doi.org/10.1016/j.nima.2015.03.068.

[26] X. Wang, et al., Chin. Phys. C 40 (2016) 086003, http://dx.doi.org/10.1088/1674-1137/40/8/086003.

[27] F. Zai-Wei, et al., Chin. Phys. C 36 (2012) 1095, http://dx.doi.org/10.1088/1674-1137/36/11/010.

[28] K.N. Yu, et al., Appl. Radiat. Isot. 59 (2003) http://dx.doi.org/10.1016/S0969-8043(03)00201-X.

[29] F.W.K. Firk, et al., Nucl. Instrum. Methods 13 (1961) 313, http://dx.doi.org/10.1016/0029-554X(61)90221-X.

[30] A.R. Spowart, Nucl. Instrum. Methods 135 (1976) 441, http://dx.doi.org/10.1016/0029-554X(76)90057-4.

[31] A.R. Spowart, Nucl. Instrum. Methods 140 (1977) 19, http://dx.doi.org/10.1016/0029-554X(77)90059-3.

[32] E.J. Fairley, et al., Nucl. Instrum. Methods 150 (1978) 159, http://dx.doi.org/10.1016/0029-554X(78)90360-9.

[33] Scintacor, https://scintacor.com/products/6-lithium-glass/.

[34] B. Jamieson, et al., Nucl. Instrum. Methods Phys. Res. A 790 (2015) 6, http://dx.doi.org/10.1016/j.nima.2015.04.022.

[35] A.W. Dalton, Nucl. Instrum. Methods Phys. Res. A 254 (1987) 361, http://dx.doi.org/10.1016/0168-9002(87)90685-1.

[36] C.W.E. van Eijk, et al., Nucl. Instrum. Methods Phys. Res. A 529 (2004) 260, http://dx.doi.org/10.1016/j.nima.2004.04.163.

[37] Hamamatsu Photonics, https://www.hamamatsu.com/resources/pdf/etd/H12700_TPMH1348Epdf.

[38] Thorlabs, Inc., http://www.thorlabs.com.

[39] R. Brun, et al., Nucl. Instrum. Methods Phys. Res. A 389 (1997) 81, See also http://root.cern.ch/.

[40] S. Agostinelli, et al., Nucl. Instrum. Methods Phys. Res. A 506 (2003) 250, http://dx.doi.org/10.1016/S0168-9002(03)01368-8.

[41] J. Allison, et al., IEEE Trans. Nucl. Sci. 53 (2006) 270, http://dx.doi.org/10.1109/TNS.2006.869826.

[42] Ray optics simulation, an open-source web application to simulate reflection and refraction of light. https://ricktu288github.io/ray-optics/.

[43] H.O. Anger, Rev. Sci. Instrum. 29 (1958) 27, http://dx.doi.org/10.1063/1.1715998.

[44] R.A. Riedel, et al., Nucl. Instrum. Methods Phys. Res. A 794 (2015) 224, http://dx.doi.org/10.1016/j.nima.2015.05.026.